Materials Advances

ROYAL SOCIETY OF CHEMISTRY

PAPER

View Article Online
View Journal | View Issue

Cite this: *Mater. Adv.*, 2024, 5, 5543

Observation of cluster spin glass behavior in thermally decomposed nanocrystalline $Sn_{0.5}Fe_{0.5}O_{2-\delta}$†

Aarti Saini,[a] Kisturi Dhanwant,[a] Mukesh Verma,[b] Sher Singh Meena,[c] Yugandhar Bitla*[b] and Ramalingam Thirumoorthi*[a]

Received 26th January 2024,
Accepted 16th May 2024

DOI: 10.1039/d4ma00077c

rsc.li/materials-advances

We report the structural and magnetic properties of nanocrystalline $Sn_{0.5}Fe_{0.5}O_{2-\delta}$ prepared by thermal decomposition of hexameric organotin ferrocenecarboxylate. The X-ray diffraction study revealed that Fe doping retains the tetragonal rutile structure of SnO_2. FTIR shows the presence of O–Sn–O stretching vibration. Microstructural investigation by FESEM and HRTEM indicated nanoparticle agglomeration and different orientations of lattice fringes with an interplanar spacing of 0.332 nm. The XPS analysis unveiled the incorporation of Fe^{3+} ions into the SnO_2 matrix. Mössbauer spectroscopy suggested the presence of Fe^{3+} ions in a distorted octahedral environment. Bulk magnetization and ac susceptibility studies assert the presence of competing ferromagnetic and antiferromagnetic interactions and a cluster spin glass state (T_g = 72 K) at low temperatures.

Introduction

Dilute magnetic semiconductors (DMS) possessing good semiconducting and magnetic properties at room temperature have attracted intense interest due to their potential practical applications.[1–3] However, the origin of magnetic interactions in DMS is ambiguous.[4–8] Most models are based on the interactions among magnetic impurities mediated *via* free carriers or oxygen ions. Defects as well as non-magnetic dopant induced ferromagnetism have also been reported.[7,8] DMS are created by partially incorporating transition metal atoms such as V, Cr, Mn, Fe, Co, Ni and so on into the semiconductors. Among oxide semiconductors, tin oxide (SnO_2), a wide band gap semiconductor owing to its high transparency, chemical stability and electrical conductivity with interesting applications in solar cells, catalysis and gas sensing, is widely explored as a promising candidate in DMS research. Therefore, room temperature ferromagnetism in transition metal-doped SnO_2 was investigated by many groups.[9–26] In particular, partially Fe doped Fe–SnO_2 has displayed large magnetic moments[24] resulting in magnetic properties suitable for spintronic applications. Both p- and n-type behaviour has been observed in Fe–SnO_2 which depends on the Fe content and operating temperature.[27] More specifically, in Fe-doped SnO_2 systems, the addition of iron induces changes in SnO_2 properties, such as the band gap value, optical transmittance, grain size, grain boundary properties, electrical and magnetic behaviors, *etc.* Furthermore, apart from the interesting magnetic properties, Fe-doped SnO_2 was used to detect ethanol,[27] carbon monoxide,[28,29] hydrogen sulphide,[30] methane,[31] acetone[32] and humidity[33] and degrade rhodamine B in aqueous solutions.[34]

The physical properties of Fe–SnO_2 can be tailored by altering its structure, composition and particle/grain size and it is sensitive to growth conditions. Various synthesis methods were employed to prepare Fe–SnO_2 samples in bulk, nanocrystalline and thin film forms.[13,15,19,24,27–50] First principles calculations suggested that the ferromagnetic state is energetically favourable compared to the antiferromagnetic state in Fe doped SnO_2.[10] Bulk Fe–SnO_2 exhibited room temperature ferromagnetism.[16] Nanocrystalline $Sn_{1-x}Fe_xO_2$ prepared by a cost-effective sol–gel route[35–38] also exhibited room temperature ferromagnetism. The maximum iron doping accomplished is 20% but the magnetic nature is unknown.[38] A polymeric modified Pechini process[39] with Sn(II)/Fe(II) and Sn(IV)/Fe(III) as starting reactants showed that Sn(IV)/Fe(III) was effective to get pure nanocrystalline $Sn_{1-x}Fe_xO_2$ (x = 0.1). A one-step co-precipitation method[40–42] was successfully employed to get an x = 0.15 sample wherein the system displayed a combination of paramagnetism and weak ferromagnetism. A similar inference was

---

[a] *Department of Chemistry, School of Chemical Sciences and Pharmacy, Central University of Rajasthan, NH8, Bandarsindri, Ajmer-305817, India. E-mail: thirumoorthi@curaj.ac.in*

[b] *Department of Physics, School of Physical Sciences, Central University of Rajasthan, NH8, Bandarsindri, Ajmer-305817, India. E-mail: y.bitla@curaj.ac.in; Tel: (+91) 7427026110*

[c] *Solid State Physics Division, Bhabha Atomic Research Centre, Mumbai 400 085, India*

† Electronic supplementary information (ESI) available. See DOI: **https://doi.org/10.1039/d4ma00077c**

obtained in the nanocrystalline $Sn_{1-x}Fe_xO_{2-\delta}$ (x = 0.1) sample prepared using the high-energy ball milling method.[43] Nanocrystalline samples prepared using the hydrothermal method[34,44,45] also exhibited ferromagnetic behaviour. Room temperature ferromagnetism ($T_c \sim 610$ K) in $Sn_{0.95}Fe_{0.05}O_2$ thin films[47] prepared using the pulsed laser deposition (PLD) method was explained using the ferromagnetic coupling of ferric ions *via* an electron trapped in oxygen vacancy (F-center exchange mechanism).[5] The magnetic moment reduces drastically as x approaches a percolation threshold of 0.25.[5] Other studies on Fe–SnO_2 thin films prepared by PLD also reported the role of oxygen vacancies near Fe atoms[48] or the importance of the double exchange mechanism[26] in $Sn_{1-x}Fe_xO_2$ ($x \leq 0.4$) in establishing the ferromagnetism in the system. In contrast, nanocrystalline $Sn_{0.8}Fe_{0.2}O_2$ films had a Fe_2O_3 impurity phase that displayed excitonic features due to 2p–3d hybridization.[49] The changes in electronic structure and magnetism of Fe–SnO_2 thin films grown by radio frequency magnetron sputtering[50,51] were attributed to bound magnetic polarons. $Sn_{1-x}Fe_xO_2$ thin films deposited by the spray pyrolysis method[52] exhibited secondary phases like β-Fe_2O_3 and β-Fe_3Sn as x changes from 0.078 to 0.396.

The increase in iron doping creates more oxygen vacancies in the SnO_2 structure. It stimulates the possibility of displaying an interesting magnetic behavior. To date, most of the studies on the $Sn_{1-x}Fe_xO_2$ system were concentrated around $x \leq 0.2$ in the bulk wherein the occurrence of ferromagnetic behaviour was ascribed to impurity band exchange or competing double and super exchange interactions or secondary phase or isolated magnetic impurity (ferric ion) interactions. A large x ($\sim$0.4) was attempted in thin films and ferromagnetic behaviour was retained[26] unlike the spin glass nature predicted by the donor-impurity model at such high doping. More so, neither higher Fe doping in nanocrystalline Fe–SnO_2 was attempted nor the nature of magnetism and underlying magnetic interactions were investigated. To the best of our knowledge, no report on $x \approx 0.5$ exists for this compound. To this end, using the thermal decomposition of the hexameric organotin drum $[n\text{BuSn(O)}O_2\text{CFc}]_6$ (Fc = ferrocenyl), we prepared nanocrystalline Fe doped SnO_2 wherein Fe and Sn are in equal proportions. In the present work, we report the structural, microstructural, X-ray photoelectron spectroscopy, Mössbauer spectroscopy, bulk magnetization and ac susceptibility studies on the nanocrystalline $Sn_{0.5}Fe_{0.5}O_{2-\delta}$ system.

Experimental details

Synthesis of the $Sn_{0.5}Fe_{0.5}O_{2-\delta}$ material

We chose the already reported, organostannoxane-supported hexaferrocene carboxylate, $[\text{nBuSn(O)}O_2\text{CFc}]_6$ (Fc = $C_5H_5FeC_5H_4$, ferrocenyl), **1** as the starting precursor for this work.[53] Because the Sn : Fe ratio is 1 : 1, achieving 50% Fe-doped SnO_2 is possible. Recently, we have successfully prepared tin(IV) oxide from the thermal decomposition of the hexameric organotin drum $[n\text{BuSn(O)}O_2\text{CR}]_6$ (R = 9-xanthenyl) by heating it to a temperature range of 600–900 °C.[54] This method has been adopted to prepare 50% Fe-doped SnO_2. Another reason for choosing **1** is that the presence of this molecule can be simply confirmed by the NMR (^{1}H and ^{119}Sn) technique, and also the molecular structure is already established. The interesting aspect of **1** is that it comprises six ferrocenecarboxylate moieties attached to a central stannoxane Sn_6O_6 core that appears to be a drum-like structure. Thermogravimetric analysis (TGA) performed provides information about the thermal stability of the obtained compound. The thermogram shows that the drum compound is stable up to 300 °C (Fig. S1, ESI†). Above this temperature, 50% decomposition occurs and after $\sim$600 °C, the compound shows stable behavior. Based on these results, the drum compound was heated at 600 °C for 2 h using a muffle furnace (Scheme 1). An orange solid obtained after thermal decomposition was crushed and powdered for further analysis.

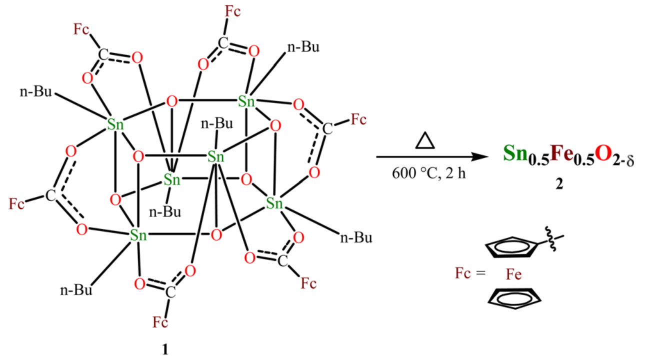

Scheme 1 Synthesis of 50% Fe doped SnO_2.

Material characterization

FT-IR spectra were recorded on a PerkinElmer instrument in the range 4000–400 cm^{-1} using KBr pellets. The FT-IR technique was used to get information about metal–oxygen stretch. The FT-IR spectrum band at 593 cm^{-1} can be related to the stretching mode vibration[55] of O–Sn–O/Sn–O–Sn/Sn–O (Fig. S2, ESI†). Thermal studies for compound **1** were carried out using an STA 6000 (PerkinElmer) instrument under a nitrogen atmosphere (20 mL min^{-1}) for 5.982 mg of sample in the temperature range of 30–700 °C. Furthermore, structural analysis with X-ray diffraction measurements was conducted in the reflection mode on an Empyrean PANalytical diffractometer (45 kV, 30 mA with Cu-K$_\alpha$ radiation with λ = 0.15406 nm). X-ray diffraction data were collected at a scanning rate of 0.0313° per second in the 2θ range from 10° to 80°. To record the X-ray diffraction (XRD) pattern, 10 mg of crushed sample was taken on zero-background silicon. The morphology of the material was examined by FE-SEM, and EDX analysis was performed using a Carl Zeiss (Ultra 55) instrument. The sample was carbon coated for FE-SEM analysis. HRTEM studies were carried out using a Tecnai G2 20 S-TWIN [FEI] instrument operated at an accelerating voltage of 200 keV. The sample was drop cast on a Cu grid for HR-TEM analysis. Oxidation states and chemical environment of elements were determined by XPS studies performed on a Kratos Axis Ultra instrument using monochromatic Mg K_α radiation. The Mössbauer spectrum of the material was recorded using a Mössbauer spectrometer operated in constant acceleration mode (triangular wave) in transmission geometry at room temperature. The source employed was ^{57}Co in the Rh matrix of strength 2 mCi. Calibration of the velocity scale was done by using an enriched α-^{57}Fe metal foil. The line width (inner) of calibration spectra was 0.26 mm s^{-1}. The isomer shift (δ) values are relative to the Fe metal foil (δ = 0.0 mm s^{-1}). Temperature and field dependent dc magnetic measurements were performed using a physical property measurement system (PPMS) (Dynacool, Quantum Design) with a vibrating sample magnetometer option (VSM). AC susceptibility measurements as a function of temperature at different frequencies were carried out using an ACMS (AC measurement system) option attached to the same PPMS setup.

Results and discussion

Fig. 1(a) shows the Rietveld refinement of room temperature powder XRD pattern of $Sn_{0.5}Fe_{0.5}O_{2-\delta}$ in the 2θ range 10°–80°. From the Rietveld refinement, it is confirmed that the sample crystallizes in a tetragonal structure (space group *P*42/*mnm*) with the lattice constants $a = b = 4.734$ Å and $c = 3.173$ Å and has a minor secondary phase of $Fe_{3-x}Sn_xO_4$. A quantitative phase analysis through the Rietveld refinement estimated the amount of the impurity phase ($Fe_{3-x}Sn_xO_4$) to be less than 2% and the impurity peak is marked with (*) in Fig. 1(a).

The average crystallite size (d) and lattice strain (ε) were estimated by employing the Williamson–Hall (WH) plot based on the equation $\beta_{\rm FWHM}\,{\rm Cos}\,\theta = k\lambda/d + 4\varepsilon\,{\rm Sin}\,\theta$, where θ is Bragg's angle, $\beta_{\rm FWHM}$ is the full width at half-maximum corresponding to Bragg's peak, k is a constant equal to 0.89 and λ is the wavelength of Cu-K_α X-ray radiation (λ = 0.154 nm). The W–H plot for $Sn_{0.5}Fe_{0.5}O_{2-\delta}$ is shown in Fig. 1(b) which gives an average crystallite size (d) of 4.30 nm and a compressive micro-strain (lattice strain ε) of 3×10^{-3}.

The crystal structure (Fig. 2) was constructed using the crystallographic information file (.cif) obtained by Rietveld refinement in 3D view with the help of VESTA software. It reveals that Sn/Fe atoms occupy the body center and corner positions of the unit cell. Every Sn/Fe atom is bonded with six oxygen atoms at octahedral positions and forms an octahedron as shown in Fig. 2b. Every unit cell consists of nine Sn/FeO_6 octahedra, out of which one is inside, and the remaining eight are at the corners of the unit cell.

Table 1 reports the structural parameters obtained from the Rietveld analysis of X-ray diffraction data collected at room temperature. In the refinement, cation occupancies were determined to be the same as the nominal values. The negligible iron oxide impurity phase in the XRD pattern implies that the magnetism and the underlying magnetic interactions are related to the properties of the host system and its oxygen off-stoichiometry, if any.

FE-SEM image was recorded to gain knowledge about the surface morphology of the material (Fig. 3a). Film-like morphology of the prepared material can be observed from the FE-SEM images. The TEM image shows the presence of agglomerated circular particles having an average diameter of ~8.5 nm (Fig. 3b). A concentric ring pattern in the selected area electron diffraction (SAED) image indicates the polycrystalline nature of the material (Fig. 3c). Lattice fringes present in the HR-TEM image (Fig. 3d) show an interplanar spacing of 0.332 nm which corresponds to the (110) plane[57] of SnO_2. Lattice fringes are rotated in different directions to show the random orientation of particles. The chemical composition revealed by EDX spectra yields Fe/(Fe + Sn) ≅ 0.5.

X-ray photoelectron spectroscopy (XPS)

XPS spectra of the sample were recorded to know the oxidation states of elements. A survey scan of the sample shows the

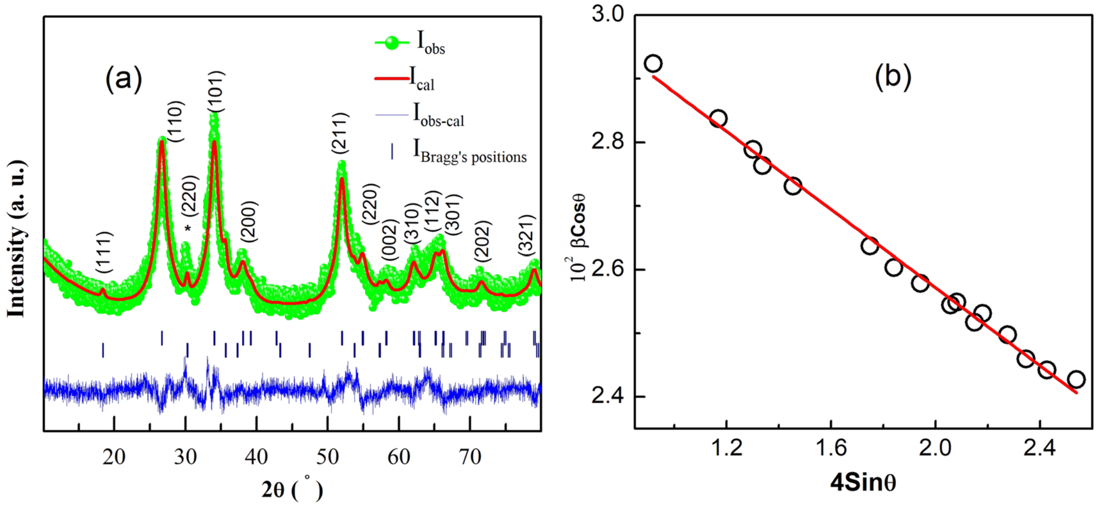

Fig. 1 (a) Rietveld refinement of room temperature XRD pattern for the $Sn_{0.5}Fe_{0.5}O_{2-\delta}$. (220) plane of $Fe_{3-x}Sn_xO_4$ is indicated by (*). (b) Williamson–Hall plot.

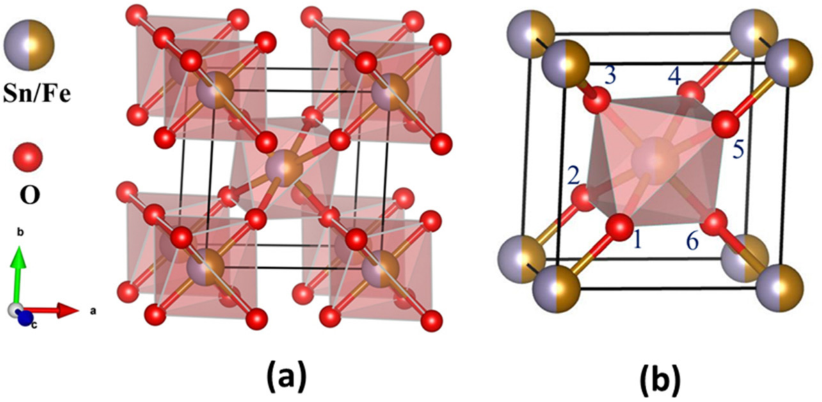

Fig. 2 Structural model of $Sn_{0.5}Fe_{0.5}O_{2-\delta}$. (a) Octahedra present in the tetragonal lattice and (b) octahedron formed by coordination of one Sn/Fe atom and six oxygen atoms.

Table 1 Structural parameters and agreement indices obtained by Rietveld refinement of the room temperature X-ray powder diffraction pattern for $Sn_{0.5}Fe_{0.5}O_{2-\delta}$

Parameter	Result
Space group	*P*42/*mnm*
Space group number	136
Crystal system	Tetragonal
No. formula units per unit cell	2
Cell parameters	
$a = b$ (Å)	4.734
c (Å)	3.173
Volume (Å^3)	71.10
Density (g cm^{-3})	5.570
Atom coordinates	
Sn/Fe (x, y, z)	0.0000, 0.0000, 0.0000
O (x, y, z)	0.2721, 0.2721, 0.0000
Occupancy	
Sn	0.50
Fe	0.49
O	1.78
Bond distance (Fig. 2b)	
Sn–O(1) (Å)	2.20
Sn–O(2) (Å)	2.20
Sn–O(3) (Å)	1.82
Sn–O(4) (Å)	2.20
Sn–O(5) (Å)	2.20
Sn–O(6) (Å)	1.82
Bond angles	
O(1)–Sn–O(2) (°)	92.24
O(1)–Sn–O(3) (°)	90.00
O(1)–Sn–O(4) (°)	180.00
O(1)–Sn–O(5) (°)	87.76
O(1)–Sn–O(6) (°)	90.00
χ^2	1.7
R_p	19.7
R_{wp}	19.0
R_e	14.2

presence of mainly carbon C(1s), oxygen O(1s), tin Sn(3d) and iron Fe(2p) peaks (Fig. 4a). A C–C bond peak was observed at 284.6 eV which is considered a reference peak (Fig. S4, ESI†). The peak at 529.4 eV in O(1s) is due to the presence of the Fe–O bond[58] and the peak at 532.9 eV may occur due to H_2O adsorbed[59] on the Fe doped SnO_2 surface (Fig. 4b). In the Sn(3d) spectrum, a doublet with peaks at 489.1 and 497.6 eV for ($3d_{5/2}$) and ($3d_{3/2}$) with a peak separation (spin–orbit splitting) of ~8.5 eV respectively suggests the presence[60] of the Sn^{4+} state of Fe/SnO_2. Another less intense deconvoluted doublet occurred at 485.8 eV and 494.1 eV assigned[56,61,62] to ($3d_{5/2}$) and ($3d_{3/2}$) respectively, indicating the presence of the Sn^{4+} oxidation state in different chemical environments (Fig. 4c). Other than these peaks, a single peak at 716.3 eV also occurred in the spectrum which belongs to Sn($3p_{3/2}$)[63,64] of the Sn^{4+} state. In the Fe(2p) spectrum, the presence of Fe^{3+} was confirmed due to the presence of peaks[65] at 713.5 eV and 726.6 eV due to ($2p_{3/2}$) and ($2p_{1/2}$) lines respectively, with a separation ($2p_{1/2}$–$2p_{3/2}$) of 13.1 eV. A satellite peak[66] for Fe^{3+} was also observed at 719.5 eV which appears highly intense due to association with the Sn $3p_{3/2}$ peak (Fig. 4d). A broad peak around 58.5–60 eV was assigned to the Fe^{3+} (3p) state (Fig. S5, ESI†). Additionally, a shoulder-type peak is also observed at about 53–56 eV. However, the absence of a doublet corresponding to Fe 2p in 709–710 eV[67] (Fig. 4) confirms no Fe^{2+} or Fe_3O_4 impurity. The oxygen deficiency content using the standard protocol turns out to be $\delta = 0.18$ which is slightly less than $\delta = 0.25$ expected from the charge neutrality of the nominal composition $Sn_{0.5}Fe_{0.5}O_{2-\delta}$.

Mössbauer spectroscopy

Knowledge of the local environment around the dopant atom is necessary to understand the underlying mechanism leading to magnetic order in the system. Therefore, a Mössbauer spectroscopy study was done to ascertain the oxidation state and local environment of Fe. The room temperature Mössbauer spectrum of $Sn_{0.5}Fe_{0.5}O_{2-\delta}$ shown in Fig. 5 exhibits a well-defined doublet indicating that the incorporated Fe-ions are paramagnetic and in the 3+ oxidation state in an octahedral environment. The presence of Fe^{2+} ions was not observed in the system. The Mössbauer spectrum measured even at a higher velocity (± 11.5 mm s^{-1}) shows no sextet (six lines Zeeman splitting pattern) related to magnetically ordered Fe^{3+} ions but a doublet. The values of spectral parameters such as δ_{IS} – the isomer shift (relative to Fe metal foil), ΔE_Q – the quadrupole splitting, Γ – the full width at half maximum, R_A – the relative spectral area

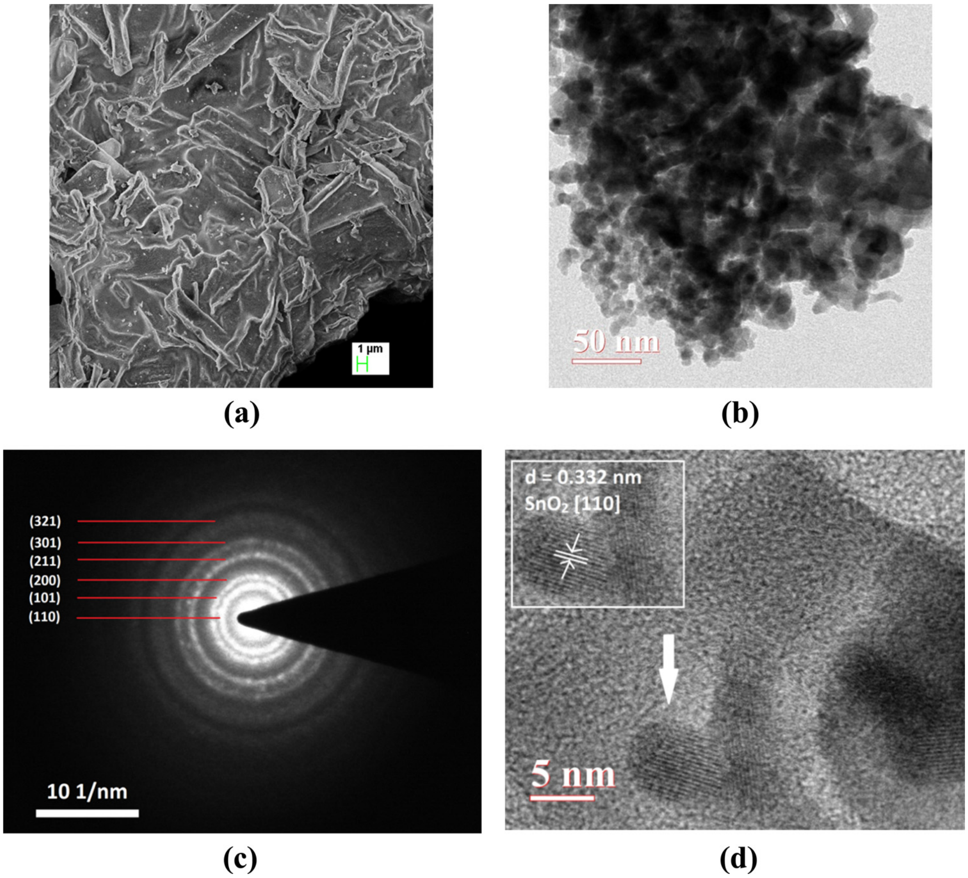

Fig. 3 (a) FE-SEM image, (b) TEM image, (c) SAED pattern, and (d) HR-TEM image of the synthesized material (the inset shows the calculated interplanar spacing).

and the co-ordination number of the Fe ion are provided in Table 2. Larger electric quadrupole splitting suggests a different Fe environment and more distorted sites in the rutile structure. This is the case of the Fe^{3+} ions in the octahedral cage of oxygen ions with relatively large concentrations of oxygen vacancies leading to a distorted environment. The data quality of the Mössbauer spectrum is poor due to the very old (low strength) Mössbauer source used for the experiment and the nano-nature of the sample. Therefore, the impurity phase of $Fe_{3-x}Sn_xO_4$ ($\sim$2%) is not visible, which should show two sextets (tetrahedral and octahedral sites) with broader line widths in the Mössbauer spectrum.

Magnetic properties

Fig. 6 shows the thermal evolution of magnetization in the temperature range of 2 K to 390 K measured in zero-field cooled (ZFC) and field-cooled (FC) modes. It can be seen that magnetization does not attain zero value even at 390 K suggesting the presence of magnetic order much above 390 K. It is interesting to see that FC magnetization at 2 K is 3 times the magnetization at 390 K. Magnetizations in ZFC and FC modes overlap with each other above a certain value of temperature, the so-called irreversibility temperature ($T_{ir} \sim 252$ K) while deviating from each other below T_{ir}. This irreversibility suggests the presence of magnetic anisotropy in the system. Irreversibility in magnetization is observed in ferromagnets, spin-glass (SG), and superparamagnetic (SPM) systems. ZFC magnetization (M_{ZFC}) exhibits a peak at $T_p = 72$ K and decreases continuously with temperature. This type of feature in M_{ZFC} is generally seen in SG and SPM systems. On the other hand, FC magnetization (M_{FC}) increases continuously below T_p suggesting the presence of antiferromagnetic interactions at low temperatures.

In Fig. 7, $M(H)$ hysteresis loops of the $Sn_{0.5}Fe_{0.5}O_{2-\delta}$ sample measured at 10 K, 50 K, and 100 K are shown. The inset shows the magnified view of MH data around the zero field. Finite coercivity (H_c) at these temperatures reflects the ferromagnetic (FM) character of the $Sn_{0.5}Fe_{0.5}O_{2-\delta}$ system. However, non-saturating MH loops at a magnetic field as high as 80 kOe suggest the presence of antiferromagnetic (AFM) correlations in the system. As the temperature increases from 10 K to 50 K, both remanent magnetization (M_r) and H_c values reduced drastically from 0.56 emu g^{-1} to 0.1 emu g^{-1} and 1500 Oe to 82 Oe, which eventually reach values of 0.02 emu g^{-1} and 22 Oe, respectively at 100 K. This is in contrast to nanocrystalline $Sn_{0.95}Fe_{0.05}O_2$ whose H_c increased with temperature[11] which was attributed to freezing of superparamagnetic domains embedded in the antiferromagnetic matrix at low temperatures. Therefore, it can be inferred that both FM and AFM interactions are present in $Sn_{0.5}Fe_{0.5}O_{2-\delta}$. The saturation magnetization at 10 K in $H = 80$ kOe reduces from 0.21 μ_B/Fe to 0.05 μ_B/Fe at 100 K.

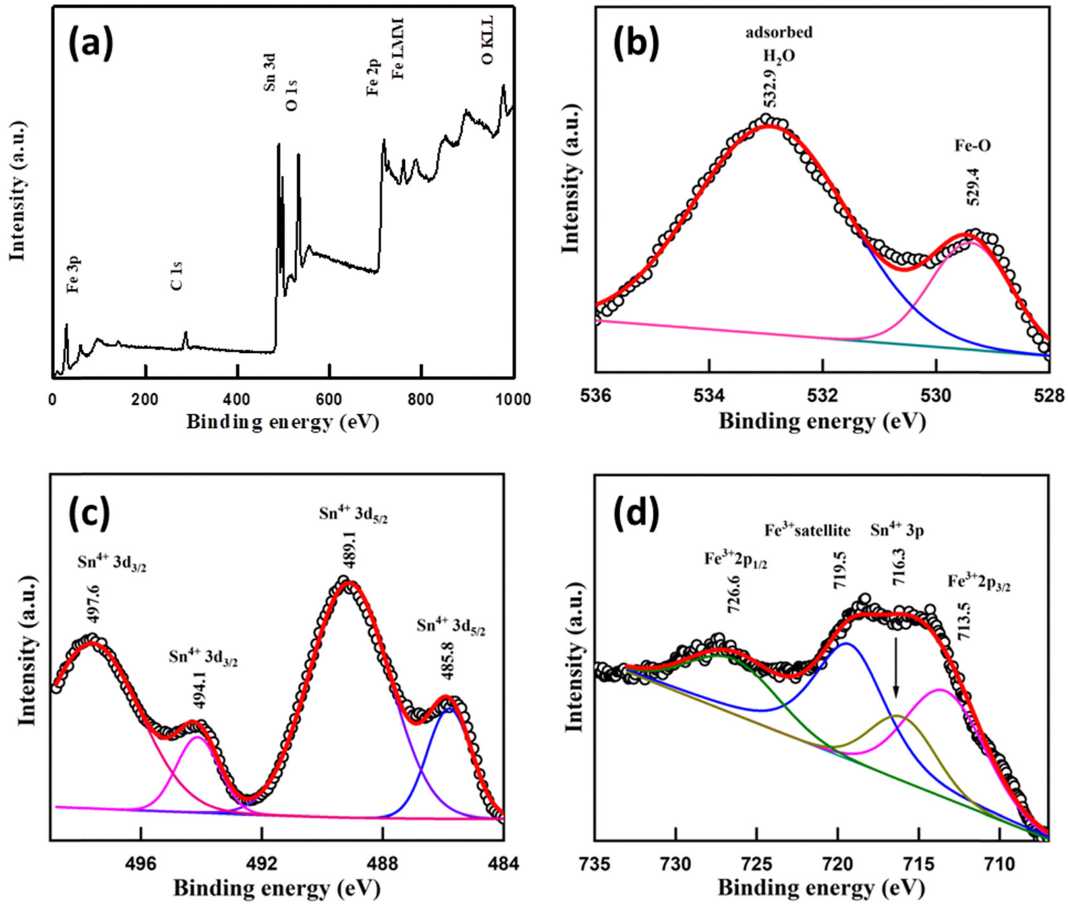

Fig. 4 XPS spectra: (a) survey scan, (b) O 1s, (c) Sn 3d and (d) Fe 2p.

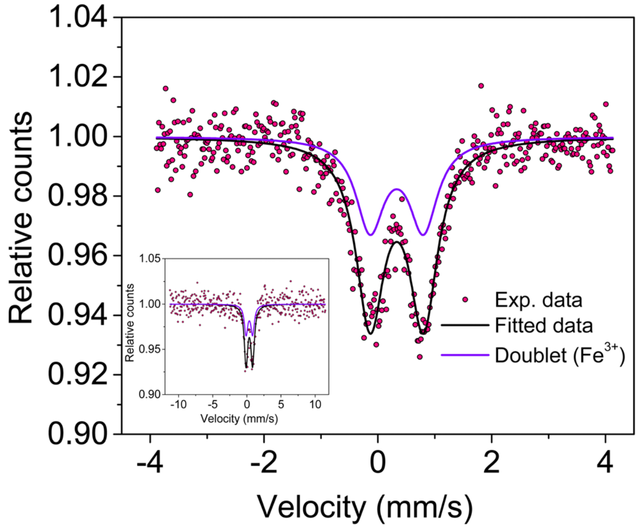

Fig. 5 Mössbauer spectrum of $Sn_{0.5}Fe_{0.5}O_{2-\delta}$ showing a doublet due to Fe^{3+} ions present in the octahedral site. The inset shows the full-scale Mössbauer spectrum.

To gain more insights into the ground state of $Sn_{0.5}Fe_{0.5}O_{2-\delta}$, ac susceptibility measurements were carried out. As shown in Fig. 8a, the real part of ac susceptibility shows a frequency dependent peak which is typical in spin glass (SG), cluster spin glass (CSG), and SPM systems. Generally, the Mydosh parameter, $\delta = \Delta T_f/T_f[\Delta \log f]$, which quantifies relative peak temperature shift per decade of frequency is employed to distinguish canonical spin glass (CG) (0.005), SG (0–0.01), CSG (0.01–0.1) and SPM (0.1–1) systems.[69–72] The estimated Mydosh parameter for $Sn_{0.5}Fe_{0.5}O_{2-\delta}$ is 0.06(1) which suggests the system to be a cluster spin glass. This value is larger than 0.0189 found in nanocrystalline $Sn_{0.95}Sn_{0.05}O_2$[11] and 0.05(1) for $Sn_{0.9}Fe_{0.1}O_{2-\delta}$[12] which reported SG behaviour. Furthermore, the frequency dependent peak temperature (T_P) is analyzed in terms of the critical slowing down (CSD) model,[69] $\tau = \tau_0\left(\frac{T_p}{T_f} - 1\right)^{-z\nu}$ where τ_0 is the relaxation time, T_f is the glass temperature and $z\nu$ is the critical exponent. As shown in Fig. 8b, the CSD model describes $T_P(\omega)$ data well yielding $\tau_0 = 4.7(3) \times 10^{-9}$ s, T_f = 67.9(8) K, and $z\nu$ = 9.2(5). For canonical SG: $\tau_0 = 10^{-12}$–10^{-13} s; for conventional spin glass: $\tau_0 = 10^{-10}$–10^{-13} s ($z\nu$ = 4–12) while $\tau_0 = 10^{-7}$–10^{-10} s for cluster spin glass.[70–73,75,76] Therefore, $Sn_{0.5}Fe_{0.5}O_{2-\delta}$ is a cluster spin glass at low temperatures.

Moreover, fit based on the Vogel–Fulcher law,[69,70] $\tau = \tau_0^* \exp\left[\frac{E_a/k_B}{T_p - T_0}\right]$, where E_a/k_B is the activation energy per

Table 2 Mössbauer spectral parameters of the $Sn_{0.5}Fe_{0.5}O_{2-\delta}$ sample at room temperature

Sample code	δ_{IS} (mm s^{-1})	ΔE_Q (mm s^{-1})	Γ (mm s^{-1})	R_A (%)	Fe-site (doublet)	Fitting quality (χ^2)
$Sn_{0.5}Fe_{0.5}O_{2-\delta}$	0.332 ± 0.006	0.938 ± 0.01	0.603 ± 0.016	100	Doublet-Fe^{3+}(VI)	1.16

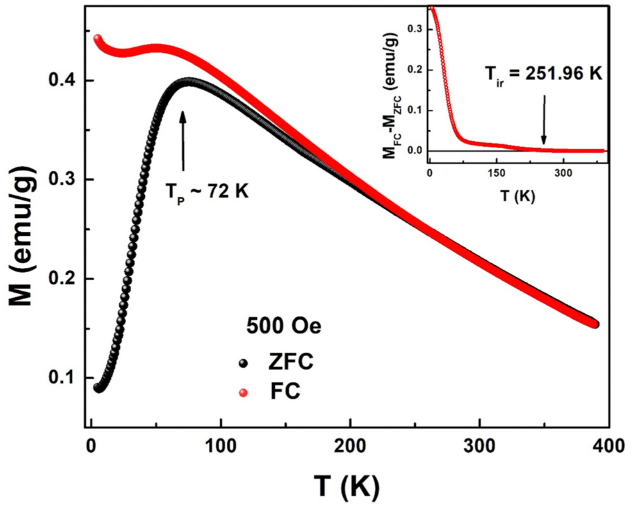

Fig. 6 Field-cooled (FC) and zero-field-cooled (ZFC) temperature dependent magnetizations at 500 Oe for $Sn_{0.5}Fe_{0.5}O_{2-\delta}$. Inset: $M_{FC}-M_{ZFC}$ as a function of temperature.

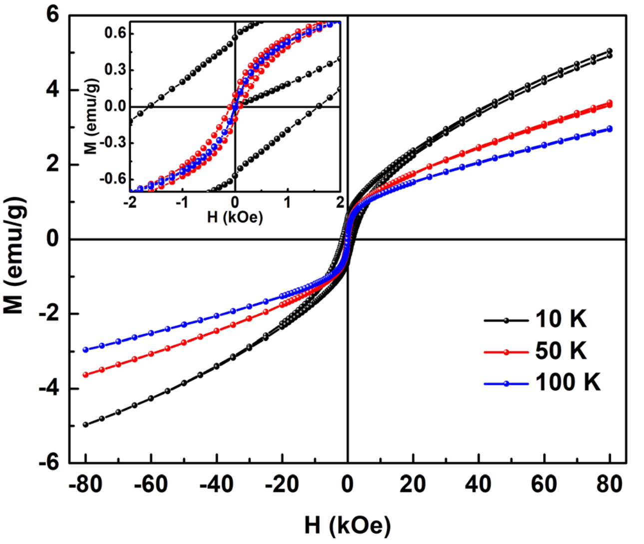

Fig. 7 *M*–*H* loops of $Sn_{0.5}Fe_{0.5}O_{2-\delta}$ at different temperatures and the inset shows the magnified view of *MH* loops at low magnetic fields.

Boltzmann constant and T_0 is the coupling strength, yield $\tau_0^* = 4.6(8) \times 10^{-11}$s, $E_a/k_B = 550.2(2)$ K and $T_0 = 53.3(2)$ K reconfirming the glassiness of the system (Fig. 8c). τ_0^* is comparable to $\tau_0 = 3 \times 10^{-10}$ s found for $Sn_{0.9}Fe_{0.1}O_{2-\delta}$[12] wherein Fe exists in +2 and +3 oxidation states. For $T_0 = 0$, this law reduces to the Arrhenius law[73] often employed for SPM systems which clearly fails in the current context. Assuming the cluster's size to be related to their coupling strength, the ratio of E_a/k_B and T_0 is used as a measure of coupling/clustering strength among the dynamic entities that freeze at T_f. $E_a/(k_BT_0) < 1$ signifies the strong coupling between the magnetic entities while $E_a/(k_BT_0) > 1$ indicates the weak coupling[68,74] In our case, $E_a/k_B \sim 10T_0$, suggests a weak coupling among the clusters and $E_a/(k_BT_0) > 1$ had been observed in cluster SG systems[75,76] which is consistent with our system. In view of the above observations, the cluster spin glass state of $Sn_{0.5}Fe_{0.5}O_{2-\delta}$ at low temperatures results due to the competing AFM and FM interactions. The FM character of the clusters is reflected in the finite values of H_c.

When a trivalent iron (Fe^{3+}: $3d^5$, $S = 5/2$) replaces a tetravalent tin in the crystallographic structure, charge neutrality ensures the creation of one oxygen vacancy per two iron ions in the lattice. Furthermore, lower ionic radii Fe^{3+} (0.069 nm) substituting for Sn^{4+} (0.083 nm) retains the rutile structure of pristine SnO_2 but disturbs the arrangement of the oxygen octahedral cage wherever it replaces the Sn ion. This is reflected in the large electric quadrupole splitting. The chemical formula based on XPS analysis can be written as $Sn^{4+}_{0.5}Fe^{3+}_{0.5}O^{2-}_{2-\delta}$ where δ is the oxygen off-stoichiometry associated with the presence of oxygen vacancies. In epitaxial thin films of $Sn_{1-x}Fe_xO_2$ (x = 0–0.4),[26] it was argued that a substantial fraction of Fe led charge compensation results in oxygen vacancies and holes. Room temperature saturation moment (coercivity) increased from 0.12 μ_B/Fe (300 Oe) for x = 0.1 to 0.71 μ_B/Fe (800 Oe) for x = 0.4. The origin of ferromagnetism[26] was attributed to dominant FM double exchange ($Fe^{2+}-O^{2-}-Fe^{3+}$ and $Fe^{3+}-O^{2-}-Fe^{2+}$) interactions over AFM superexchange ($Fe^{3+}-O^{2-}-Fe^{3+}$ and $Fe^{2+}-O^{2-}-Fe^{2+}$) interactions. On the other hand, the donor impurity band exchange mechanism[5] was proposed to explain the existence of large moments and ferromagnetism in dilute ferromagnetic oxides. In particular, in the case of the Fe–SnO_2 system, F-center exchange mechanism[47] was invoked wherein F-centers created due to oxygen vacancies (□) trap spin polarized electrons leading to ferromagnetic $Fe^{3+}-\square-Fe^{3+}$ interactions that dominate over existing antiferromagnetic $Fe^{3+}-O^{2-}-Fe^{3+}$ superexchange interactions. These shallow donor electrons form bound magnetic polarons coupling the adjacent magnetic cations within their hydrogenic radius (ν). For large enough ν, $\delta > \delta_p$ (polaron percolation threshold) and $x < x_p$ (cation percolation threshold), this model[5] predicts the occurrence of room temperature ferromagnetism. For the $Sn_{1-x}TM_xO_2$ system, $\delta_p = 0.001$ and $x_p = 0.25$ where TM is the magnetic transition metal. When $x > x_p$, antiferromagnetic or ferrimagnetic behavior is predicted as there are continuous paths throughout the lattice joining nearest-neighbor cations so much so that the net magnetic moment drastically vanishes. This impurity band model fails when δ increases, as the donor state merges with the bottom of the

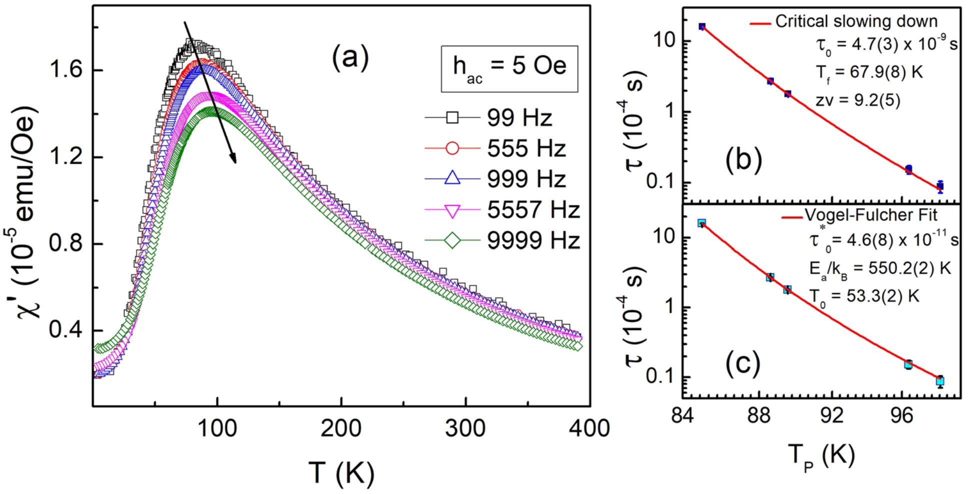

Fig. 8 (a) Real part of the ac susceptibility as a function of temperature at a fixed driving field amplitude and different frequencies. Frequency-dependent peak temperature T_P fit using (b) the critical slowing down model and (c) the Vogel–Fulcher law for $Sn_{0.5}Fe_{0.5}O_{2-\delta}$.

conduction band and the system behaves as a spin glass system whose description can be understood in terms of the Ruderman–Kittel–Kasuya–Yosida (RKKY) exchange interaction. In the present case of highly doped $Sn_{0.5}Fe_{0.5}O_{2-\delta}$ (x = 0.5 and δ = 0.25), the $Fe^{3+}-Fe^{3+}$ interaction pathways are nearest neighbour (AFM $Fe^{3+}-O^{2-}-Fe^{3+}$ and FM $Fe^{3+}-\square-Fe^{3+}$) and next-nearest neighbour ($Fe^{3+}-O^{2-}-Sn^{4+}-O^{2-}-Fe^{3+}$, $Fe^{3+}-\square-Sn^{4+}-O^{2-}-Fe^{3+}$, $Fe^{3+}-O^{2-}-Sn^{4+}-\square-Fe^{3+}$ and $Fe^{3+}-\square-Sn^{4+}-\square-Fe^{3+}$) interactions. Among them, the nearest neighbour interactions (antiferromagnetic $Fe^{3+}-O^{2-}-Fe^{3+}$ and ferromagnetic $Fe^{3+}-\square-Fe^{3+}$) play a pivotal role in governing the magnetic behavior of the dilute Fe-doped SnO_2 system ($x < x_p$). However, in the $Sn_{0.5}Fe_{0.5}O_{2-\delta}$ ($x > x_p$ and $\delta > \delta_p$) system, neither the donor impurity band exchange nor RKKY exchange mechanisms could explain the observed cluster spin glass behavior at low temperatures. More so, the contributions from next-nearest neighbour interactions, however small, become significant in addition to the existing nearest-neighbour (AFM $Fe^{3+}-O^{2-}-Fe^{3+}$ and FM $Fe^{3+}-\square-Fe^{3+}$) interactions as the probability of finding an Sn^{4+} ion as the nearest neighbor to Fe^{3+} ion is 1/2. Eventually, these competing interactions lead to the cluster glass behavior at low temperatures. The finite coercivity at temperatures $T < T_g$ corresponds to those of the FM clusters embedded in the AFM matrix. The dominant AFM correlations of the matrix are reflected in the upturn in magnetization at low temperatures. We believe that as temperature increases above T_g, the AFM state survives and may transform into a paramagnetic state above 390 K.

Conclusions

A thermally decomposed nanocrystalline $Sn_{0.5}Fe_{0.5}O_{2-\delta}$ sample was characterized by XRD, FTIR, FESEM, HRTEM, XPS, Mössbauer spectroscopy, bulk magnetization and ac susceptibility measurements. The Rietveld refined XRD data showed the single-phase compound (≈98%) exhibiting a tetragonal rutile structure and an average crystallite size of 4.3 nm. FTIR confirmed the presence of stretching vibration mode of the O–Sn–O group at ~593 cm^{-1}. FESEM displayed a platelet-like surface while HRTEM showed nanoparticle agglomeration and reconfirmed polycrystallinity through the SAED pattern. EDX confirmed the presence of Fe and Sn in equal proportions. XPS and Mössbauer studies verified the trivalent nature of Fe and its distorted oxygen environment due to oxygen vacancies. The magnetic study (M–H, M–T and ACS) showed evidence for (i) competing ferromagnetic and antiferromagnetic interactions involving Fe^{3+} ions and (ii) cluster spin glass state at low temperatures and magnetic ordering temperature much above room temperature.

Author contributions

A. S.: investigation, formal analysis, validation, and visualization. K. D.: investigation. M. V.: investigation, visualization, and formal analysis. S. S. M.: investigation, formal analysis, and visualization. Y. B.: investigation, formal analysis, methodology, visualization, and validation. R. T.: conceptualization, methodology, resources, supervision, and funding acquisition. All the authors contributed to writing the manuscript.

Conflicts of interest

There are no conflicts of interest to declare.

Acknowledgements

AS is thankful to CURAJ for the University Fellowship. KD & MV gratefully acknowledge UGC for Senior Research Fellowships. RT thanks the Council of Scientific and Industrial Research, India (grant no. 01(2970)/19/EMR-II dated: 20th June 2019 to Ramalingam Thirumoorthi). We are thankful to IISc Bangalore for FE-SEM and XPS analysis, MNIT Jaipur for HR-TEM, BARC Mumbai for Mössbauer spectroscopy, and CURAJ for instrumental facilities (PXRD and PPMS).

References

1 G. A. Prinz, Magnetoelectronics, *Science*, 1998, **282**, 1660–1663.

2 Y. Matsumoto, M. Murakami, T. Shono, H. Hasegawa, T. Fukumura, M. Kawasaki, P. Ahmet, T. Chikyow, S. Koshihara and H. Koinuma, Room-Temperature Ferromagnetism in Transparent Transition Metal–Doped Titanium Dioxide, *Science*, 2001, **291**, 854–856.

3 S. A. Wolf, D. D. Awschalom, R. A. Buhrman, J. M. Daughton, S. V. Molnar, M. L. Roukes, A. Y. Chtchelkanova and D. M. Treger, Spintronics: A Spin-Based Electronics Vision for the Future, *Science*, 2001, **294**, 1488–1495.

4 I. S. Elfimov, A. Rusydi, S. I. Csiszar, Z. Hu, H. H. Hsieh, H. J. Lin, C. T. Chen, R. Liang and G. A. Sawatzky, Magnetizing Oxides by Substituting Nitrogen for Oxygen, *Phys. Rev. Lett.*, 2007, **98**, 137202.

5 J. M. D. Coey, M. Venkatesan and C. B. Fitzgerald, Donor impurity band exchange in dilute ferromagnetic oxides, *Nat. Mater.*, 2005, **4**, 173.

6 A. S. Risbud, N. A. Spaldin, Z. Q. Chen, S. Stemmer and R. Seshadri, Magnetism in polycrystalline cobalt-substituted zinc oxide, *Phys. Rev. B: Condens. Matter Mater. Phys.*, 2003, **68**, 205202.

7 M. Venkatesan, C. B. Fitzgerald, J. G. Lunney and J. M. D. Coey, Anisotropic ferromagnetism in substituted zinc oxide, *Phys. Rev. Lett.*, 2004, **93**, 177206.

8 I. S. Elfimov, S. Yunoki and G. A. Sawatzky, Possible Path to a New Class of Ferromagnetic and Half-Metallic Ferromagnetic Materials, *Phys. Rev. Lett.*, 2002, **89**, 216403.

9 K. Nomura, Magnetic properties and oxygen defects of dilute metal doped tin oxide based semiconductor, *Croat. Chem. Acta*, 2015, **88**, 579–590.

10 X. L. Wang, Z. X. Dai and Z. Zeng, Search for ferromagnetism in SnO_2 doped with transition metals (V, Mn, Fe, and Co), *J. Phys.: Condens.Matter*, 2008, **20**, 045214.

11 K. C. Verma and R. K. Kotnala, Realizing ferromagnetic ordering in SnO_2 and ZnO nanostructures with Fe, Co, Ce ions, *Phys. Chem. Chem. Phys.*, 2016, **18**, 17565.

12 C. E. R. Torres, A. F. Cabrera and F. H. Sánchez, Magnetic behavior of nanoclusters of Fe-doped SnO_2, *Physica B*, 2007, **389**, 176–179.

13 D. Manikandan and R. Murugan, Genesis and tuning of ferromagnetism in SnO_2 semiconductor nanostructures: Comprehensive review on size, morphology, magnetic properties and DFT investigations, *Prog. Mater. Sci.*, 2022, **130**, 100970.

14 S. J. Liu, C. Y. Liu, J. Y. Juang and H. W. Fang, Room-temperature ferromagnetism in Zn and Mn codoped SnO_2 films, *J. Appl. Phys.*, 2009, **105**, 013928.

15 X. L. Wang, Z. X. Dai and Z. Zeng, Search for ferromagnetism in SnO_2 doped with transition metals (V, Mn, Fe, and Co), *J. Phys.: Condens. Matter*, 2008, **20**, 045214.

16 C. B. Fitzgerald, M. Venkatesan, A. P. Douvalis, S. Huber, J. M. D. Coey and J. Bakas, SnO_2 doped with Mn, Fe or Co: Room temperature dilute magnetic semiconductors, *J. Appl. Phys.*, 2004, **95**, 7390–7392.

17 J. Zhang, R. Skomski, L. P. Yue, Y. F. Lu and D. J. Sellmyer, Structure and magnetism of V-doped SnO_2 thin films: effect of the substrate, *J. Phys.: Condens. Matter*, 2007, **19**, 256204.

18 N. H. Hong, J. Sakai, W. Prellier and A. Hassini, Transparent Cr-doped SnO2 thin films: ferromagnetism beyond room temperature with a giant magnetic moment, *J. Phys.: Condens.Matter*, 2005, **17**, 1697–1702.

19 A. Punnoose, J. Hays, A. Thurber, M. H. Engelhard, R. K. Kukkadapu, C. Wang, V. Shutthanandan and S. Thevuthasan, Development of high-temperature ferromagnetism in SnO_2 and paramagnetism in SnO by Fe doping, *Phys. Rev. B: Condens. Matter Mater. Phys.*, 2005, **72**, 054402.

20 A. Punnoose, J. Hays, V. Gopal and V. Shutthanandan, Room-temperature ferromagnetism in chemically synthesized $Sn_{1-x}Co_xO_2$ powders, *Appl. Phys. Lett.*, 2004, **85**, 1559–1561.

21 S. B. Ogale, R. J. Choudhary, J. P. Buban, S. E. Loftland, S. R. Shinde, S. N. Kale, V. N. Kulkarni, J. Higgins, C. Lanci, J. R. Simpson, N. D. Browning, S. D. Sarma, H. D. Drew, R. L. Greene and T. Venkatesan, High Temperature Ferromagnetism with a Giant Magnetic Moment in Transparent Co-doped $SnO_{2-\delta}$, *Phys. Rev. Lett.*, 2003, **91**, 077205.

22 N. H. Hong, A. Ruyter, W. Prellier, J. Sakai and N. T. Huong, Magnetism in Ni-doped SnO_2 thin films, *J. Phys.: Condens.-Matter*, 2005, **17**, 6533–6538.

23 S. Harbeck, A. Szatvanyi, N. Barsan, U. Weimar and V. Hoffmann, DRIFT studies of thick film un-doped and Pd-doped SnO_2 sensors: temperature changes effect and CO detection mechanism in the presence of water vapour, *Thin Solid Films*, 2003, **436**, 76–83.

24 C. V. Komen, A. Thurber, K. M. Reddy, J. Hays and A. Punnoose, Structure–magnetic property relationship in transition metal (M = V, Cr, Mn, Fe, Co, Ni) doped SnO_2 nanoparticles, *J. Appl. Phys.*, 2008, **103**, 07D141.

25 T. Sabergharesou, T. Wang, L. Ju and P. V. Radovanovic, Electronic structure and magnetic properties of sub-3 nm diameter Mn-doped SnO_2 nanocrystals and nanowires, *Appl. Phys. Lett.*, 2013, **103**, 012401.

26 H.-S. Kim, L. Bi, G. F. Dionne, C. A. Ross and H. J. Paik, Structure, magnetic and optical properties, and Hall effect of Co- and Fe-doped SnO_2 films, *Phys. Rev. B: Condens. Matter Mater. Phys.*, 2008, **77**, 214436.

27 K. Galatsis, L. Cukrov, W. Wlodarski, P. McCormick, K. Kalantarzadeh, E. Comini and G. Sberveglieri, p- and n-type Fe-doped SnO_2 gas sensors fabricated by the mechanochemical processing technique, *Sens. Actuators, B*, 2003, **93**, 562–565.

28 G. Sberveglieri, C. Perego, F. Parmigiani and G. Quattroni, $Sn_{1-x}Fe_xO_y$: a new material with high carbon monoxide sensitivity, *Sens. Actuators, B*, 1994, **20**, 163–167.

29 X.-T. Yin and X.-M. Guo, Selectivity and sensitivity of Pd-loaded and Fe-doped SnO_2 sensor for CO detection, *Sens. Actuators, B*, 2014, **200**, 213–218.

30 M. V. Vaishampayan, R. G. Deshmukh, P. Walke and I. S. Mulla, Fe-doped SnO_2 nanomaterial: A low temperature hydrogen sulfide gas sensor, *Mater. Chem. Phys.*, 2008, **109**, 230–234.

31 S. Bose, S. Chakraborty, B. K. Ghosh, D. Das, A. Sen and H. S. Maiti, Methane sensitivity of Fe-doped SnO_2 thick films, *Sens. Actuators, B*, 2005, **105**, 346–350.

32 J. Hu, Y. Wang, W. Wang, Y. Xue, P. Li, K. Lian, L. Chen, W. Zhang and S. Zhuiykov, Enhancement of the acetone sensing capabilities to *ppb* detection level by Fe-doped three-dimensional SnO_2 hierarchical microstructures fabricated via a hydrothermal method, *J. Mater. Sci.*, 2017, **52**, 11554–11568.

33 D. Toloman, A. Popa, M. Stan, C. Socaci, A. R. Biris, G. Katona, F. Tudorachec, I. Petrilad and F. Iacomi, Reduced graphene oxide decorated with Fe doped SnO_2 nanoparticles for humidity sensor, *Appl. Surf. Sci.*, 2017, **402**, 410–417.

34 W. B. H. Othmen, N. Sdiri, H. Elhouichet and M. Férid, Study of charge transport in Fe-doped SnO_2 nanoparticles prepared by hydrothermal method, *Mater. Sci. Semicond. Process.*, 2016, **52**, 46–54.

35 J. Kaur, J. Shah, R. K. Kotnala and K. C. Verma, Raman spectra, photoluminescence and ferromagnetism of pure, Co and Fe doped SnO_2 nanoparticles, *Ceram. Int.*, 2012, **38**, 5563–5570.

36 S. Sambasivam, B. C. Choi and J. G. Lin, Intrinsic magnetism in Fe doped SnO_2 nanoparticles, *J. Solid State Chem.*, 2011, **184**, 199–203.

37 M. S. Pereira, T. S. Ribeiro, F. A. S. Lima, L. P. M. Santos, C. B. Silva, P. T. C. Freire and I. F. Vasconcelos, Synthesis and properties of $Sn_{1-x}Fe_xO_2$ nanoparticles obtained by a proteic sol–gel method, *J. Nanopart. Res.*, 2018, **20**, 212.

38 W. B. H. Othmen, Z. B. Hamed, B. Sieber, A. Addad, H. Elhouichet and R. Boukherroub, Structural and optical characterization of p-type highly Fe-doped SnO_2 thin films and tunneling transport on SnO_2:Fe/p-Si heterojunction, *Appl. Surf. Sci.*, 2018, **434**, 879–890.

39 J. J. Beltran, L. C. Sánchez, J. Osorio, L. Tirado, E. M. Baggio-Saitovitch and C. A. Barrero, Crystallographic and magnetic properties of Fe-doped SnO_2 nanopowders obtained by a sol–gel method, *J. Mater. Sci.*, 2010, **45**, 5002–5011.

40 K. K. Pandimeena, M. C. Robert and S. Saravanakumar, Energy gap tuning, ferromagnetic switching, visualization of electron density and bonding in dilute magnetic semiconductor Fe-doped SnO_2, *Optik*, 2023, **287**, 171091.

41 R. Adhikari, A. K. Das, D. Karmakar, T. V. C. Rao and J. Ghatak, Structure and magnetism of Fe-doped SnO_2 nanoparticles, *Phys. Rev. B: Condens. Matter Mater. Phys.*, 2008, **78**, 024404.

42 S. Ferrari, L. G. Pampillo and F. D. Saccone, Magnetic properties and environment sites in Fe doped SnO_2 Nanoparticles, *Mater. Chem. Phys.*, 2016, **177**, 206–212.

43 M. S. Pereira, G. M. S. L. Mendes, T. S. Ribeiro, M. R. Silva and I. F. Vasconcelos, Influence of Thermal-Treatment Effects on the Structural and Magnetic Properties of $Sn_{1-x}Fe_xO_2$ Nanopowders Produced by Mechanical Milling, *J. Supercond. Novel Magn.*, 2020, **33**, 1721–1728.

44 W. B. H. Othmen, B. Sieber, C. Cordier, H. Elhouichet, A. Addad, B. Gelloz, M. Moreau, A. Barras, M. Férid and R. Boukherroub, Iron addition induced tunable band gap and tetravalent Fe ion in hydrothermally prepared SnO_2 nanocrystals: Application in photocatalysis, *Mater. Res. Bull.*, 2016, **83**, 481–490.

45 W. B. H. Othmen, B. Sieber, H. Elhouichet, A. Addad, B. Gelloz, M. Moreau, S. Szunerits and R. Boukherroub, Effect of high Fe doping on Raman modes and optical properties of hydrothermally prepared SnO_2 nanoparticles, *Mater. Sci. Semicond. Process.*, 2018, **77**, 31–39.

46 L. Peng and T. Liu, Effects of Fe Doping on Defects, Structural Disorder, and Optical and Magnetic Properties of SnO_2 Nanoparticles, *J. Supercond. Novel Magn.*, 2021, **34**, 1287–1296.

47 J. M. D. Coey, A. P. Douvalis, C. B. Fitzgerald and M. Venkatesan, Ferromagnetism in Fe-doped SnO_2 thin films, *Appl. Phys. Lett.*, 2004, **84**, 1332–1334.

48 C. E. R. Torres, L. Errico, F. Golmar, A. M. M. Navarro, A. F. Cabrera, S. Duhalde, F. H. Sánchez and M. Weissmann, The role of the dopant in the magnetism of Fe-doped SnO_2 films, *J. Magn. Magn. Mater.*, 2007, **316**, e219–e222.

49 W. Yu, K. Jiang, J. Wu, J. Gan, M. Zhu, Z. Hu and J. Chua, Electronic structures and excitonic transitions in nanocrystalline iron-doped tin dioxide diluted magnetic semiconductor films: an optical spectroscopic study, *Phys. Chem. Chem. Phys.*, 2011, **13**, 6211–6222.

50 M. K. Jaiswal, R. Kumar, D. Kanjilal, C. L. Dong, C. L. Chen, K. Asokan and S. Ojha, Studies of dense electronic excitation-induced modification in crystalline Fe-doped SnO_2 thin films, *Appl. Surf. Sci.*, 2015, **332**, 726–735.

51 Y. Fu, N. Sun, L. Feng, S. Wen, Y. An and J. Liu, Local structure and magnetic properties of Fe-doped SnO_2 films, *J. Alloys Compd.*, 2017, **698**, 863–867.

52 M. M. B. Mohagheghi, N. Shahtahmasebi, M. R. Alinejad, A. Youssefi and M. S. Saremi, Fe-doped SnO_2 transparent semi-conducting thin films deposited by spray pyrolysis technique: Thermoelectric and p-type conductivity properties, *Solid State Sci.*, 2009, **11**, 233–239.

53 V. Chandrasekhar, S. Nagendran, S. Banzal, M. A. Kozee and D. R. Powell, An Iron Wheel on a Tin Drum: A Novel Assembly of a Hexaferrocene Unit on a Tin–Oxygen Cluster, *Angew. Chem., Int. Ed.*, 2000, **39**, 1833–1835.

54 V. Chandrasekhar, R. Thirumoorthi, K. Dhanwant and A. Saini, Photophysical studies of organostannoxane supported hexafluorophore assemblies, *Inorg. Chim. Acta*, 2021, **522**, 120378.

55 S. P. Chand, Effect of pH Values on the Structural, Optical and Electrical Properties of SnO_2 Nanostructures, *Optik*, 2019, **181**, 768–778.

56 Y. Wang, Y. Deng, L. Fan, Y. Zhao, B. Shen, D. Wu, Y. Zhou, C. Dong, M. Xing and J. Zhang, In situ strategy to prepare PDPB/SnO_2 p–n heterojunction with a high photocatalytic activity, *RSC Adv.*, 2017, **7**, 24064–24069.

57 H. Ji, Y. Fan, J. Yan, Y. Xu, X. She, J. Gu, T. Fei, H. Xu and H. Li, Construction of SnO_2/graphene-like g-C_3N_4 with enhanced visible light photocatalytic activity, *RSC Adv.*, 2017, **7**, 36101–36111.

58 L. Li, P. Ma, S. Hussain, L. Jia, D. Lin, X. Yin, Y. Lin, Z. Cheng and L. Wang, FeS_2/carbon hybrids on carbon cloth: a highly efficient and stable counter electrode for dye-sensitized solar cells, *Sustainable Energy Fuels*, 2019, **3**, 1749–1756.

59 V. Kumar, V. Kumar, S. Som, J. H. Neethling, M. Lee, O. M. Ntwaeaborwa and H. C. Swart, The role of surface and deep-level defects on the emission of tin oxide quantum dots, *Nanotechnology*, 2014, **25**, 135701.

60 M. Wang, G.-M. Weng, G. Yasin, M. Kumar and W. Zhao, A high-performance tin phosphide/carbon composite anode for lithium-ion batteries, *Dalton Trans.*, 2020, **49**, 17026–17032.

61 W. Li, F. Yang, B. Huang, Z. Liu, H. Meng, J. Zheng, B. Zeng, J. Yang, Y. Li, S. Xiao, Q. Chen and X. Zhao, Monodisperse SnO_2/Co_3O_4 nanocubes synthesized via phase separation and their advantages in electrochemical Li-ion storage, *Ionics*, 2020, **26**, 6125–6132.

62 Q. Gao, P. Li, S. Ding, H. He, M. Cai, X. Ning, Y. Cai and M. Zhang, Cu_2Se-ZnSe heterojunction encapsulated in carbon fibers for high-capacity anodes of sodium-ion batteries, *Ionics*, 2020, **26**, 5525–5533.

63 X. Liu, J. Zhang, X. Guo, S. Wang and S. Wu, Core–shell α–Fe_2O_3@SnO_2/Au hybrid structures and their enhanced gas sensing properties, *RSC Adv.*, 2012, **2**, 1650–1655.

64 X. Zhao, T. Wen, J. Zhang, J. Ye, Z. Ma, H. Yuan, X. Ye and Y. Wang, Fe-Doped SnO_2 catalysts with both BA and LA sites: facile preparation and biomass carbohydrates conversion to methyl lactate MLA, *RSC Adv.*, 2017, **7**, 21678–21685.

65 Q. Zhang, Y. Fan, W. Wang, N. Liu and J. Guan, Enhanced Water Oxidation Activity by Introducing Gallium into Cobalt-Iron Oxide System, *ChemElectroChem*, 2020, **7**, 118–123.

66 P. Nag, S. Banerjee, Y. Lee, A. Bumajdad, Y. Lee and P. S. Devi, Sonochemical Synthesis and Properties of Nanoparticles of $FeSbO_4$, *Inorg. Chem.*, 2012, **51**, 844–850.

67 A. Rajan, M. Sharma and N. K. Sahu, Assessing magnetic and inductive thermal properties of various surfactants functionalised Fe_3O_4 nanoparticles for hyperthermia, *Sci. Rep.*, 2020, **10**, 15045.

68 P. Bag, P. R. Baral and R. Nath, Cluster spin-glass behavior and memory effect in $Cr_{0.5}Fe_{0.5}Ga$, *Phys. Rev. B*, 2018, **98**, 144436.

69 Y. Bitla, S. N. Kaul and L. F. Barquín, Nonlinear susceptibilities as a probe to unambiguously distinguish between canonical and cluster spin glasses, *Phys. Rev. B: Condens. Matter Mater. Phys.*, 2012, **86**, 094405.

70 G. Benka, A. Bauer, P. Schmakat, S. Säubert, M. Seifert, P. Jorba and C. Pfleiderer, Interplay of itinerant magnetism and spin-glass behavior in Fe_xCr_{1-x}, *Phys. Rev. Mater.*, 2022, **6**, 044407.

71 M. R. Chowdhury, M. S. Seehra, P. Pramanik, S. Ghosh, T. Sarkar and B. Weise, S. Thota. Antiferromagnetic short-range order and cluster spin-glass state in diluted spinel $ZnTiCoO_4$, *J. Phys.: Condens. Matter*, 2022, **34**, 275803.

72 S. K. Jena, T. Sarkar, M. RoyChowdhury, B. Weise, Y. Qi and S. Thota, Slow spin dynamics of cluster spin-glass spinel $Zn(Fe_{1-x}Ru_x)_2O_4$: role of Jahn–Teller active spin-1/2 Cu^{2+} ions at B-sites, *J. Phys.: Condens. Matter*, 2022, **34**, 405801.

73 R. Kumar, P. Yanda and A. Sundaresan, Cluster-glass behavior in the two-dimensional triangular lattice Ising-spin compound $Li_2Mn_3O_7$, *Phys. Rev. B*, 2021, **103**, 214427.

74 S. Shtrikman and E. P. Wohlfarth, The theory of the Vogel-Fulcher law of spin glasses, *Phys. Lett. A*, 1981, **85**, 467–470.

75 M. Roy-Chowdhury, M. S. Seehra and S. Thota, Optimized analysis of the AC magnetic susceptibility data in several spin-glass systems using the Vogel–Fulcher and Power laws, *AIP Adv.*, 2023, **13**, 115020.

76 S. Ghosh, D. C. Joshi, P. Pramanik, S. K. Jena, S. Pittala, T. Sarkar, M. S. Seehra and S. Thota, Antiferromagnetism, spin-glass state, H–T phase diagram, and inverse magnetocaloric effect in Co_2RuO_4, *J. Phys.: Condens. Matter*, 2020, **32**, 485806.